

Effect of Weld Consumable Conditioning on the Diffusible Hydrogen and Subsequent Residual Stress and Flexural Strength of Multipass Welded P91 Steels



CHANDAN PANDEY, M.M. MAHAPATRA, PRADEEP KUMAR, and N. SAINI

P91 steel weld joint was prepared using the shielded metal arc welding process and four different conditions of weld consumable that provide the different levels of diffusible hydrogen in deposited metal. In the present research, the effects of diffusible hydrogen content on the flexural strength, lower critical stress, and tensile strength of P91 steel welds were also determined with respect to different electrode conditions. To investigate the effect of diffusible hydrogen on multipass welding, top and root side flexural tests were performed. The residual stresses (axial stress and transverse stress) were also measured using the blind hole drilling method for different conditions of welding consumable. The peak value of residual stresses was measured at the center of the weld fusion zone. The maximum value of transverse stress was measured to be 355 MPa for case II (6.21 mL/100 g of diffusible hydrogen), while the maximum axial stress was about 218 MPa for case IV (12.43 mL/100 g of diffusible hydrogen). A three-dimensional finite element simulation was also performed to predict the residual stress distribution and thermal profile along the welded joint. The experimentally determined residual stresses correlated well with the numerically estimated residual stresses. The diffusible hydrogen content was not observed to have any significant effect on the residual stresses. The corrected residual stress values were also predicted by considering the plasticity-induced error. However, the flexural performance of the welded joint was affected by the diffusible hydrogen content. The top and root flexural strength was measured to be optimum for the low level of diffusible hydrogen content, and the values decreased with an increase in diffusible hydrogen content.

<https://doi.org/10.1007/s11663-018-1314-8>

© The Minerals, Metals & Materials Society and ASM International 2018

I. INTRODUCTION

THE modified 9Cr-1Mo steel designated as P91 is preferred for high-temperature applications in modern supercritical power plants due to its excellent microstructure stability and mechanical properties with good workability and weldability. The P91 steel is also well known for its superior physical and thermal properties.^[1,2] It also shows good microstructure stability during high-temperature exposure.^[3–5] The

weldability of such steel depends upon a suitable heat treatment and welding procedure. In the as-received condition, P91 steel processes the tempered martensitic structure with $M_{23}C_6$ -type carbide precipitates mainly rich in Fe, Cr, and Mo. The heterogeneous microstructure during the welding cycle results in poor creep rupture life of the welded joint as compared to the virgin metal.^[6] The weldability of the P91 steel depends on the microstructure of the weld fusion zone, trapped diffusible hydrogen, and residual deformation. However, the residual deformation and the microstructure can be optimized up to a level by using the proper weld heat treatments. The microstructure of the weld fusion zone deals with the untempered martensite and sometimes residue of austenite and δ ferrite patches. The softening of the weld fusion zone is performed by heat treatment, as reported in earlier research.^[7] However, the control of diffusible hydrogen in deposited metal-assisted cold cracking or hydrogen-induced cracking (HIC) is difficult. The combination of susceptible microstructure, diffusible hydrogen, and residual stress might lead to the catastrophic failure of the weld joint and term as HIC.

CHANDAN PANDEY, PRADEEP KUMAR, and N. SAINI are with the Department of Mechanical and Industrial Engineering, Indian Institute of Technology Roorkee, Uttarakhand 247667, India. Contact e-mail: chandanpy.1989@gmail.com M.M. MAHAPATRA is with the School of Mechanical Sciences, Indian Institute of Technology, Bhubaneswar, Odisha 751013, India.

Manuscript submitted November 24, 2017.

Article published online July 10, 2018.

The welding-induced distortion and residual deformation depend on many parameters including welding process and parameters, groove geometry, phase transformation, and properties of the material. The induced tensile residual stresses in the welded component result in HIC, buckling deformation, brittle fracture, stress corrosion cracking, and reduction in other mechanical properties.^[8–10] The researchers performed much work on the effect of the welding process parameter and heat treatment on residual deformation in the weld joint of P91 steel. The effect of the solid-phase transformation plays an important role in determining the magnitude of the residual stress, and softening of the structure also affects the magnitude of the residual stress. The effect of postweld heat treatment (PWHT) on residual deformation of P91 welded pipe was studied by Pandey *et al.*^[11] They also studied the effect of the groove geometry on residual stresses and shrinkage stresses. A drastic reduction in the magnitude of the residual stress was reported as a result of the PWHT. Yaghi *et al.*^[12] simulated the residual stresses developed in the weld and heat-affected zone (HAZ) in butt-welded pipe of 50-mm thickness and 145-mm outer diameter, using the finite element (FE) method. The phase transformation characteristic of the weld cycle was used for FE analysis. The volumetric change during the solid-state phase transformation (SSPT) from austenite to martensite and the change in yield stress are used in the modeling. The PWHT resulted in a drastic reduction in the magnitude of the residual, and it was attributed to temperature-dependent mechanical properties and redistribution of the residual stresses as a result of creep of material. The PWHT holding time also had a drastic effect on residual stress, and it was reduced with an increase in holding time. A similar study was performed by Zubairuddin *et al.*^[13] They also reported the effect of SSPT from austenite to martensite on the magnitude of the residual stress and the effect of SSPT from austenite to martensite on the magnitude of the residual stress. The research reported that phase transformation did not even affect the magnitude of the residual stress or also sometimes the nature of the residual stresses.^[14] A study of the effect of martensitic start temperature on the magnitude of residual stresses found that low martensitic transformation start temperature might be the cause of the reduction in magnitude of tensile residual stress developed in the weld joint.^[15] The low martensitic transformation start temperature resulted in the formation of compressive stresses that counterbalanced the magnitude of tensile stress in the weld zone. The preheating also produced a noticeable effect on the magnitude of residual stress, and it was reported to decrease after preheating.^[13] The residual stress distribution in the girth of P91 welded pipe and the effect of the PWHT were studied by Paddea *et al.*^[16] The maximum residual stress of 600 MPa was measured near the boundary of the base zone and HAZ that also considered the prone area for Type IV cracking.^[17] The tensile hydrostatic stress was also maximum near the vicinity of the HAZ. The PWHT resulted in a drastic reduction in the magnitude of the residual stress, as reported by other researchers. In the final weld pass, the compressive mode of the residual stress was measured. Venkata *et al.*^[18] studied

electron-beam-welded P91 steel weld joints, their residual stress distribution in electron-beam-welded P91 steel plate and the effect of PWHT on their magnitude. The experimentally measured residual stress values using the neutron diffraction technique were compared with the values obtained using FE simulation. The PWHT below the A_{c1} temperature was recommended for the minimum residual stresses. The PWHT effect on the magnitude of the residual stress in the root and cap of the weld was also studied by Chuvas *et al.*^[19] A comparative study of the impact of welding processes on the magnitude of residual stress was performed by Kulkarni *et al.*^[20] Residual stress estimation in P91 welded structures is also reported by Kim *et al.*^[21] using the neutron diffraction technique. The experimentally obtained results fairly matched with the numerically obtained values. The effect of the welding sequence on residual deformation was studied by Sattari-Far and Javadi.^[22] The welding sequence led to diametrical variation. Pipe wall thickness was reported to be a great influence on residual stress deformation.^[23] The effect of diffusible hydrogen content on the mechanical performance of ferritic-martensitic steel was also studied.^[24] Varying diffusible hydrogen content in the single-pass-deposited metal was shown to have a great influence on mechanical behavior. Mechanical performance was reported to be decreased with the increase in the level of diffusible hydrogen content. However, a rough estimation was made and a study related to the effect of diffusible hydrogen content on mechanical properties of multipass shield metal-arc-welded P91 steel joints was carried out. Albert *et al.*^[26] and Yue^[27] studied the negative influence of diffusible hydrogen content on the lower critical stress (LCS) of the steel joints.

From the literature survey, it is clear that studies of the effect of diffusible hydrogen content on LCS were conducted by many researchers. The various welding process parameters, specimen thicknesses, SSPTs during welding, and effects of start and stop positions of welding and PWHT on residual stresses were also studied. However, a study examining the effect of diffusible hydrogen content on residual stress and flexural strength of multipass welded P91 steels is not readily available in the literature. In the present research work, P91 steel plate joints were prepared using the shielded metal arc welding (SMAW) process for four different conditions of weld consumables, *i.e.*, different levels of diffusible hydrogen content. The effects of diffusible hydrogen content on residual deformation and flexural strength of multipass P91 steel weldments were studied. The residual stresses were calculated using the blind hole drilling method with consideration of the plasticity-induced error.

II. EXPERIMENTAL DETAILS

A. Material and Welding Procedure

P91 steel plates having dimensions 200 mm × 200 mm × 20 mm were machined from the supplied cast and forged P91 steel plate for joining purposes. The chemical compositions of the plate and mechanical

properties are depicted in Tables I.^[28] and II,^[29] respectively. Plates of dimension 200 mm × 200 mm × 18 mm were machined for welding purposes. P91 plate after the groove preparation is shown in Figure 1(a). The details of groove dimension are shown in the top of Figure 1(a). The bevel angle, root face height, and root gap were 37.5 deg, 1.5, and 1.5 mm, respectively. Figure 1(b) shows the weld pass arrangement for making the weld joints. Before welding, the preheating of the plate was carried out at 300 °C. To overcome the distortion of the plate during welding, the plate was tacked from both sides, as shown in Figure 1(c). The root pass was carried out on the top and bottom sides using the gas tungsten arc welding (GTAW) process. The plate after root passes is shown in Figures 1(d) and (e). The subsequent filling passes were performed *via* the SMAW process by using the welding consumable rod of diameter 4 mm and designated as 9CrMoV-N (E9015-B9). The chemical compositions of GTAW filler wire and SMAW filler rod are depicted in Table I. The plate after the completion of welding is shown in Figure 1(f). Table III shows the welding process parameters for case I. For the GTAW root pass and SMAW filler pass, heat-transfer efficiencies are considered as 0.65 and 0.87, respectively.^[30] The heat input is given by Eq. [1]^[31]:

$$Q = \frac{\eta \times V \times I}{TS}, \quad [1]$$

where Q is heat input (kJ/mm), η is heat-transfer efficiency, V is voltage (V), I is current (amp), and TS is travel speed (mm/s).

Welding was done for the different conditions of weld consumable, as depicted in Table IV.^[25,32] The number of filler passes used for welding for cases I, II, III, and IV were 14, 13, 14, and 14, respectively. Study of the diffusible hydrogen level on SMAW-deposited metal for four different conditions of weld consumable was reported by Dong^[23] and Pandey and Mahapatra.^[24] Multipass welding of P91 steel weldments was performed in the similar condition of weld consumable. However, it is difficult to measure the hydrogen content in the multipass-welded joint. The hydrogen content for the different conditions of weld consumable is depicted in Table IV.

B. Measurement of Residual Stress in P91 Welded Plate

The blind hole drilling method was used to measure the residual stresses per ASTM E837-13 standard. TML FRS-2-1, three-element strain gage rosettes were pasted to measure the residual stress in the weld fusion zone, HAZ, and root face. At the center of the strain gage rosette, a hole of 2-mm diameter was created by using the end mill cutter. Residual longitudinal and axial stress at the top and root face of P91 plate weld was estimated using the ASTM E837-13 standard. The weld plate with strain gage rosette is shown in Figures 2(a) and (b). The plate after the blind hole drill is shown in Figure 2(c).

In the blind hole drilling method, the relief strains are measured using the strain gage rosette that was attached to the specimen surface to make a blind hole at the center of it. The principle stresses and their directions are mainly related to the relieved strains. In the blind hole drilling method, the stress concentration factor and plasticity lead to overestimation of strain data.^[33] To overcome their effects during residual stress measurement, the induced error was estimated for the strain gage FRS-2-11.

C. Numerical Analysis

For thermomechanical FE analysis of welding, temperature-dependent physical and thermal properties of base and weld metal were used. To perform the FE analysis, rate-independent thermal-elasto-plastic material and a large displacement model were used. The FE analysis was performed in two steps. Initially, the transient temperature distribution was estimated using thermal analysis. After the transient thermal analysis, nonlinear structure analysis was performed to predict the residual stress distribution in the welded material.

1. FE model and material properties

To predict the residual stress in the conventional V-groove welded plate, a two-dimensional (2-D) axisymmetric FE model was used. To accommodate the steep temperature rise in the weld, fine meshing was carried out in the weld and adjacent area of the weld as compared to the remaining part of the FE model. In the FE model, each pass consisted of several numbers of elements at which heat flux was applied per the welding pass sequence. The temperature-dependent properties used for the FE simulation are per Reference 34. A comparative study was performed to study the location of the fusion boundary from the weld centerline in the actual weld cross section and 2-D FE model. Five different locations were selected from the plate inner and outer surfaces, and the results are depicted in Table V.

2. Thermal analysis

Transient thermal and nonlinear structure analyses were performed to determine the residual stress in P91 welded plate. In multipass welding, the heating and cooling cycles were divided into several steps. FE solver ANSYS was used to perform the transient thermal analysis and nonlinear structural analysis for each load step of the heating and cooling cycles. For the nonlinear structural analysis, transient temperature analysis was used as the input parameter. The heat flux assumed to be distributed was Gaussian in nature.

The heat input during the welding processes and the feed rate were used in deciding the size of passes in the FE model. In the welding process, heat loss primarily occurs as convection and radiation. The combined effect was estimated using Eq. [2].^[35,36]

Table I. Chemical Composition of As-received Cast and Forged P91 Steel, SMAW Filler Rod, and GTAW Filler Wire (Weight Percent)^[28]

Element	Chemical Composition (Weight Percent)												
	C	Mn	W	S	Si	Cr	Mo	V	N	Ni	Cu	Nb	Ti
Cast and forged P91 steel	0.02	0.69	0.026	0.02	0.19	8.16	0.71	0.23	< 0.02	0.31	0.03	0.05	< 0.02
SMAW filler rod	0.08 to 0.13	0.40 to 1.0	—	max 0.02	0.20 to 0.50	8 to 10	0.85 to 1.1	0.15 to 0.30	0.03 to 0.07	0.4 to 1.0	—	0.04 to 0.08	—
GTAW filler wire	0.12	0.50	—	0.019	0.30	9.0	0.90	0.20	< 0.02	0.50	—	0.06	< 0.02

$$h_c = 24.1 \times 10^{-4} \epsilon T^{1.61} \quad [2]$$

The element birth technique was applied to simulate each pass of the weld. In this method, each pass activated at a particular time at which the molten metal was deposited. Brickstad *et al.*^[37] performed a similar study. A reasonable molten zone size (1340 °C to 1390 °C) is obtained along the weld groove edges using the proper heat flux. The boundary at which the temperature is in the range of 850 °C to 950 °C is considered as the HAZ. In multipass welding, weld pass was not allowed to cool up to ambient temperature. The interpass temperature was maintained in the temperature range of 250 °C to 300 °C. Hence, for the subsequent passes, the initial temperature may not be ambient. The softening temperature resulted in a minute effect on the final results of modeling. Liu *et al.*^[38] used a softening temperature of 1200 °C for multipass steel pipe welds.

D. Flexural Test and Fracture Surface Morphology

For flexural tests for both the top and root face, specimens with dimensions 160 mm × 12.5 mm × 10 mm were machined from the welded plate. The schematic of the flexural test specimen is shown in Figure 3. The flexural test was performed on both the face and root side with the transverse specimen at a constant crosshead speed of 1 mm/min. The bend radius of the three-point bend roller was 10 mm. Each data point of flexural tests represented the average of at least two specimens. The fracture flexural test specimen was analyzed using an FE scanning electron microscope (SEM).

III. RESULTS AND DISCUSSION

A. Microstructure and Macrostructure Analysis

The typical micrograph of as-received P91 is characterized by lath blocks, packets, block boundaries, and coarse M₂₃C₆-type carbide and fine MX-type carbide and carbonitride precipitates.^[40] The other precipitates reported are Cr, Fe, Mo-rich M₇C₃, Fe-rich M₃C, M₂C, and Cr₂N.^[25] The fact that the coarse precipitates are mainly arrested along the boundaries shows the coarsening nature, while intergranular precipitates of MX and M₂₃C₆ types show higher stability against coarsening, as shown in Figure 4(a). The optical micrograph shows the typical tempered martensitic microstructure. In the as-received condition, columnar laths in the form of packets or groups are found inside the grain boundaries, as shown in Figure 4(b). Table II shows the mechanical properties of the P91 steel.

A cross-sectional view of the multipass butt-welded joint is shown in Figure 5(a). In P91 weld joints, the different zones formed are the weld fusion zone, coarse-grained-HAZ (CG-HAZ), fine-grained-HAZ (FG-HAZ), and intercritical HAZ (IC-HAZ). Typical micrographs for subzones of P91 weldments are shown in Figures 5(b) through (e). In the weld fusion zone, complete dissolution of precipitates causes the martensitic structure to have strong strength, hardness, and poor

Table II. Mechanical Properties of Cast and Forged P91 Steel in As-received State^[29]

Mechanical Properties	Yield Strength (MPa)	Tensile Strength (MPa)	Elongation (Pct)	Hardness (HV)	Impact Toughness (J)
Grade 91 steel	455 ± 10	655.5 ± 6.36	22.08 ± 0.247	231 ± 5.38	96 ± 5
Minimum required	450	650 to 750	15	—	30

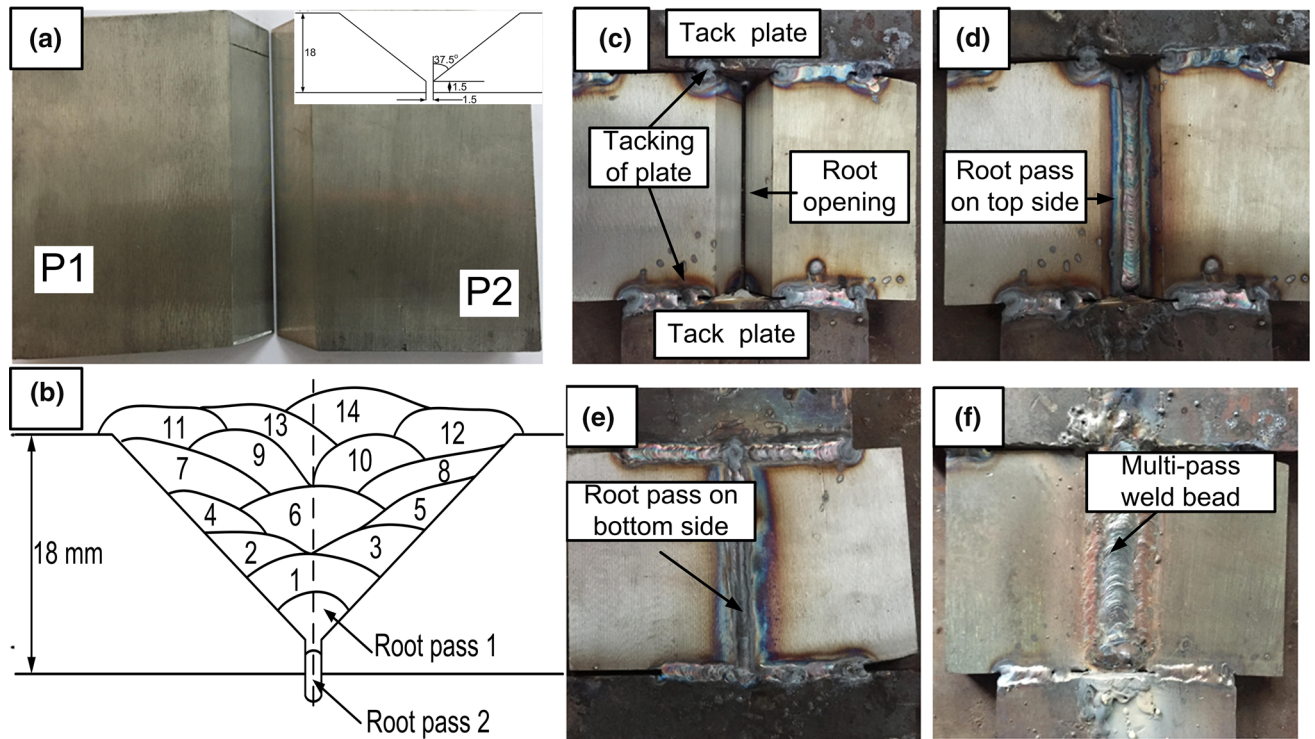


Fig. 1—(a) Machined and grooved plate with groove geometry, (b) weld pass arrangement (all dimensions in millimeters), (c) plate after tacking, (d) plate after root pass on top side, (e) plate after root pass on bottom side, and (f) plate after completion of filling pass.

Table III. Welding Process Parameters Used in the Welding P91 Plates

Passes	Welding Process	Voltage (V)	Travel Speed S (mm/s)	Current (Amps)
Root pass (1, 2)	GTAW	12 to 16	2.14	110 to 120
Filling passes (14)	SMAW	21 to 25.6	3.20 to 5.36	140 to 151

Table IV. Electrode Condition Used for Measurement of Diffusible Hydrogen in Different Cases^[25,32]

Test Case	Electrode Condition	Mean Diffusible Hydrogen Content (H_{Mercury}) (mL/100 g)
I	electrode baked at 300 °C for 2 h	3.92
II	electrode used in unbaked condition	6.21
III	after baking electrode dipped in 10W oil before welding for 10 min	9.18
IV	after baking electrode dipped in 20 W oil before welding for 10 min	12.43

toughness. The columnar laths are clearly seen from the micrograph. CG-HAZ (Figure 5(c)) looks different from the weld fusion zone. At high temperature, the complete dissolution of precipitates results in coarse austenite grain

formation because the boundaries become free from the pinning effect of the precipitates. The complete dissolution of precipitates in the weld fusion zone and CGHAZ resulted in high-strength lath martensitic structure

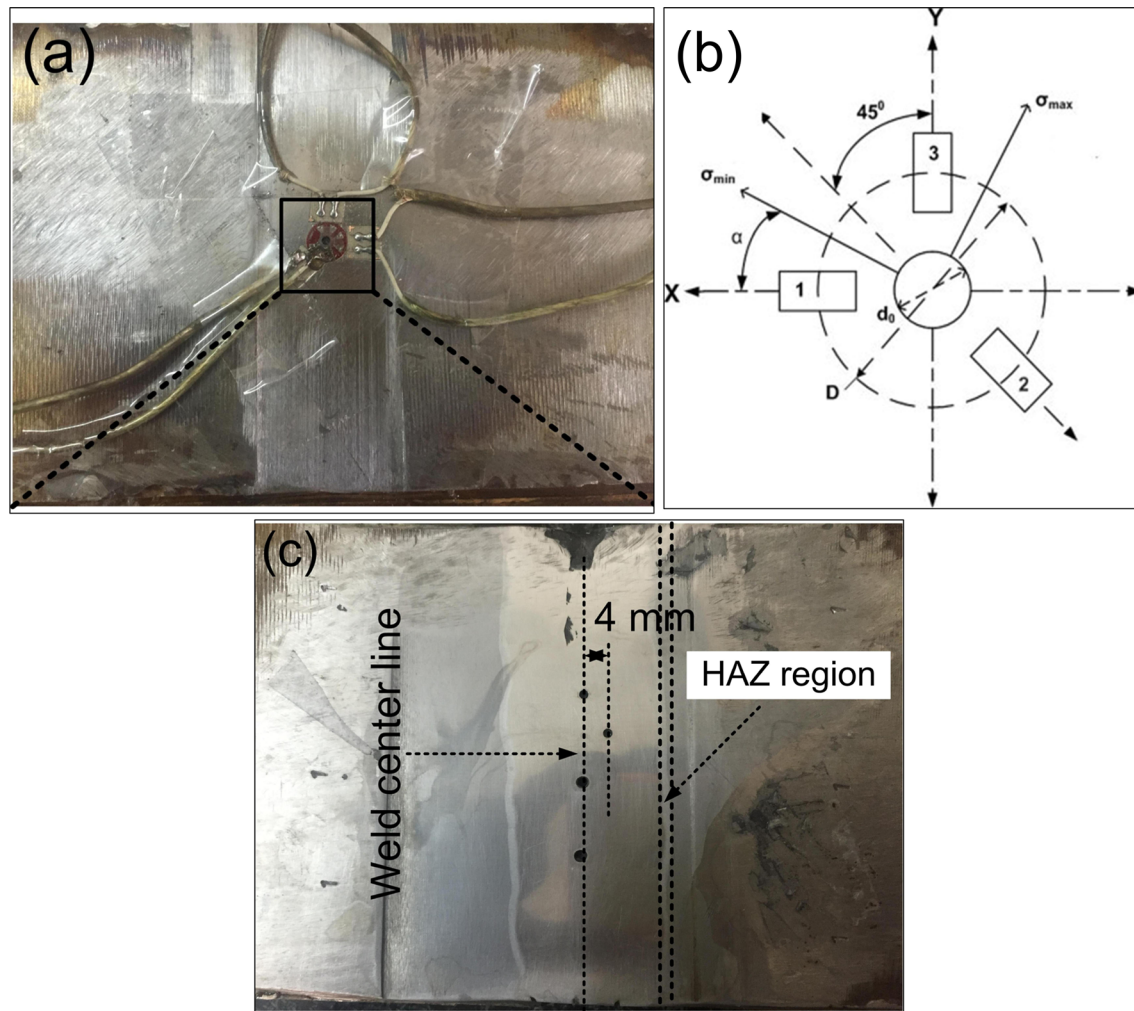


Fig. 2—(a) Attachment of strain gage rosettes at the weld center, (b) schematic of strain gage rosette, and (c) plate after the blind hole drilling at weld fusion zone center and at 4 mm away from it.

formation. The temperature achieved by the FG-HAZ was not sufficient to completely dissolve all the precipitates. Hence, FG-HAZ was characterized by the mixed structure of tempered and untempered laths with some amount of undissolved coarse precipitates, as shown in Figure 5(d). The undissolved precipitates were also responsible for fine structure formation due to their pinning effect on subgrain boundaries. The most interesting region of weldments is the intercritical-heat-affected zone (IC-HAZ). In multipass P91 weldments, it is difficult to distinguish IC-HAZ from FG-HAZ because of the narrow width of about $200\ \mu\text{m}$.^[41] To locate the IC-HAZ by using SEM is also quite difficult. After welding, new prior austenite grain boundaries (PAGBs) were formed within the IC-HAZ. The PAGBs are derived by tracing the retained $M_{23}C_6$ -type precipitates on boundaries (Figure 5(e)). In the IC-HAZ, the new precipitates are formed during the weld cooling cycle and coarse $M_{23}C_6$ precipitates are retained from the as-received metal. The newly formed untempered martensite contributed to higher dislocation density and strain magnitude compared to the retained tempered martensite of the base metal.

Microhardness variation across the multipass welded P91 joint is shown in Figure 6. A great variation in the hardness value of the fusion zone was noticed. The hardness varied from 400 to 457 HV with an average of 422 HV. The variation in hardness of the weld fusion zone was mainly due to the autotempering effect of subsequent weld passes. The hardness of subzones was mainly governed by the dissolution of precipitates.^[41,42] In the weld fusion zone and CGHAZ, the higher hardness value was attributed to the higher weight percentage of C and N in the solution matrix as a result of the precipitates' dissolution. The FG-HAZ exhibited lower hardness because of the lower strength of martensite, *i.e.*, incomplete dissolution of precipitates. A sudden dip was noticed in the hardness profile at the base and HAZ boundary. The region is defined as a so-called soft zone or IC-HAZ. In the IC-HAZ, the hardness was 214 HV, which is slightly more than that in the overtempered base zone. The presence of hardness gradients across the weldments led to poor performance in service condition. The variation in hardness of subzones was also confirmed by the microstructure.

Table V. Comparison of Fusion Boundary

Point	Distance from Weld Root to Weld Top (in mm)	Conventional Groove Fusion Boundary	
		From Weld Cross Section Center (mm)	In FEM Model Weld Cross Section Center (mm)
A	0	2.2	2
B	5	3.20	4.18
C	10	7.15	8.90
D	15	12.40	14.89
E	18	14.50	15.60

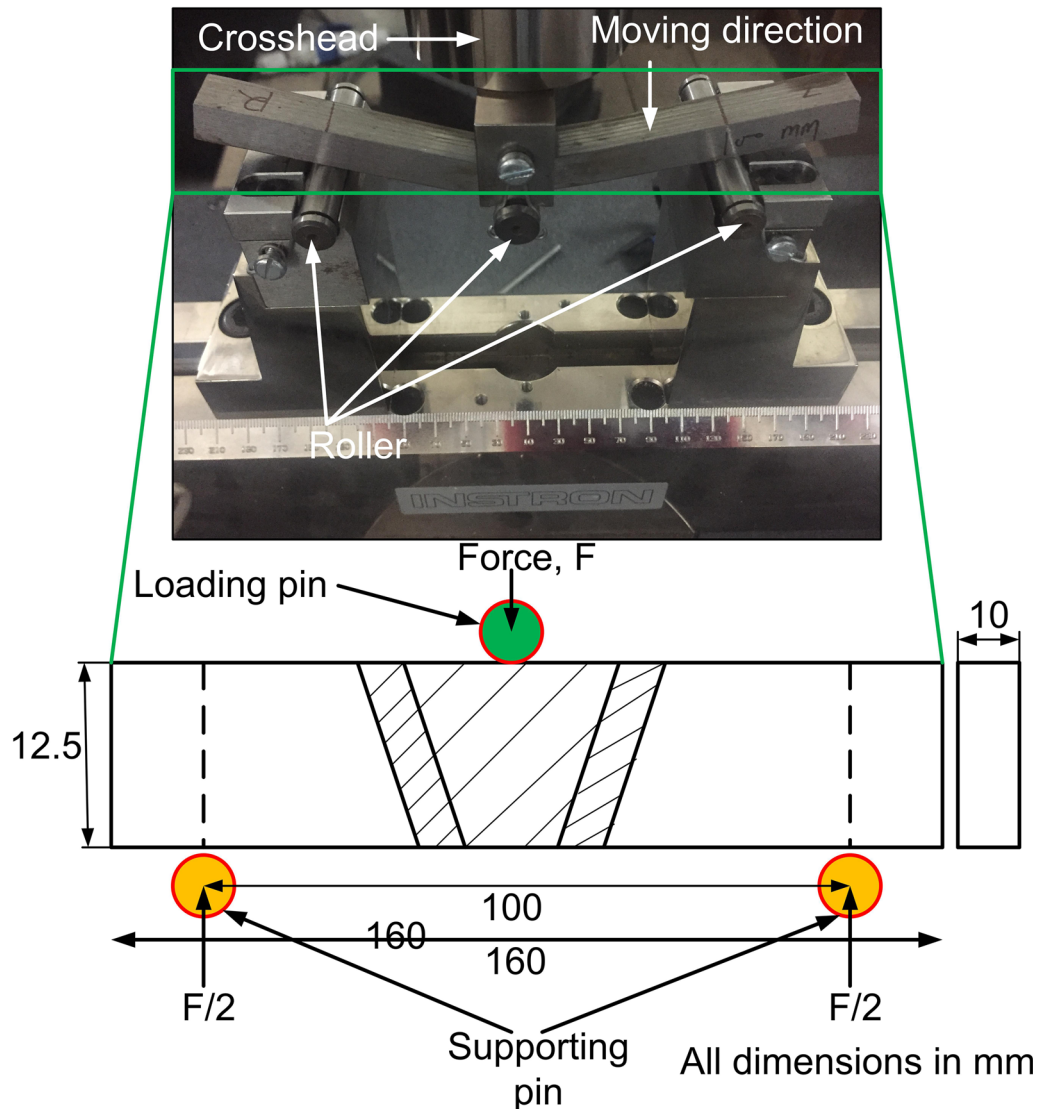


Fig. 3—Flexural test setup.

B. Residual Stress in P91 Welded Plate

1. Residual stress estimation using the experimental method

In the blind hole drilling method, the stress concentration factor and plasticity lead to overestimation of strain data. To overcome the effect of stress concentration and plasticity during the residual stress

measurement, the induced error was estimated for the strain gage FRS-2-11 having a drilled hole of 2-mm diameter, as given in Eqs. [3] and [4]. The residual stress for different conditions of the welded plate is presented in Table VI. The effect of diffusible hydrogen content was not found in any fixed pattern on residual stress distribution. The residual stresses

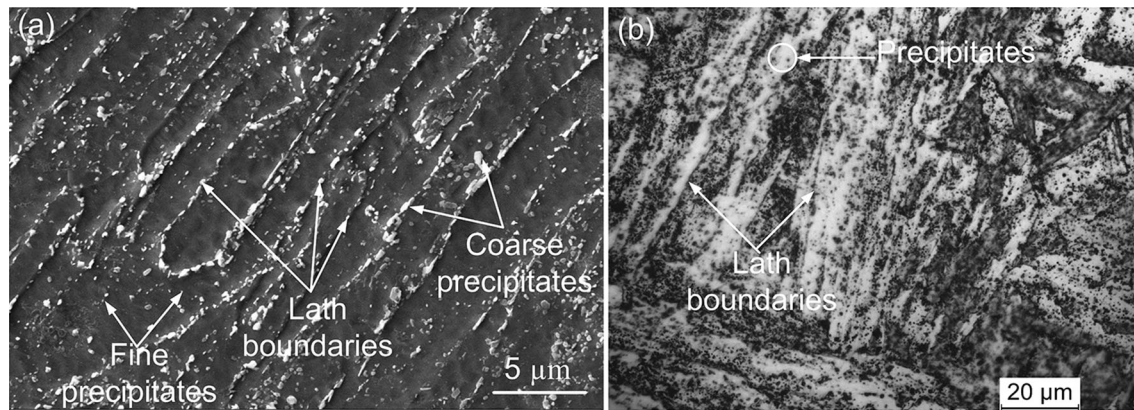


Fig. 4—(a) Secondary electron micrograph of as-received steel and (b) optical micrograph.^[25,39]

measured for the low level of diffusible hydrogen (3.916 mL/100 g) and for a high level of diffusible hydrogen (12.43 mL/100 g) were almost similar. Maximum transverse and axial stresses were measured at the center of the weld fusion zone. As one moves away from the weld center, the magnitude of residual stresses is observed to decrease. In case I, the transverse and axial stresses were measured to be 295 and 205 MPa, respectively, while the corrected transverse and axial stresses were measured at 196 and 102 MPa, as given in Table VI. The maximum value of the transverse stress was measured to be 355 MPa for case II, while the maximum axial stress was about 218 MPa for case IV. The magnitude of the transverse and axial stresses was measured to be of a tensile nature for all cases. Residual stresses measured at 4-mm distance from the center of the weld fusion zone were observed to be less compared to stresses measured at the weld center, but the difference in magnitude was much less. The magnitude of residual stresses in the HAZ was observed to be similar to that measured 4 mm away from the weld center. In the HAZ, the maximum magnitudes of axial and transverse stresses were 196 and 231 MPa for cases I and III, respectively. The transverse and axial stresses measured at the root of the welded plate were observed to be compressive in nature. The maximum magnitude was measured for case IV, as shown in Table VI. The residual stresses measured at the center of the weld were maximum as a result of the SSPT. The center of the weld deals with the last pass. However, at 4 mm away, the 11th or 12th pass was performed, which was autotempered as a result of the subsequent 13th or 14th pass. The last bead was deposited on the weld center, as shown in Figure 1(b). Hence, the extent of autotempering at 4 mm from the weld centerline was approximately similar to that of the HAZ. The less microstructural difference between the upper portion of the weld at a distance of 4 mm and the HAZ was considered to arrive at this most probable reasoning.

The corrected axial and transverse stresses were measured using Eqs. [3] and [4].^[33] A significant difference was observed in the ASTM measured value and the corrected value of residual stresses, as given in Table VI.

$$\sigma_L = -32.7 - 241\sigma_{Lastm}/\sigma_y - 0.006\sigma_{Tastm} + 1.2\sigma_{Lastm} \quad [3]$$

$$\sigma_T = -6.21 + 404.58\sigma_{Tastm}/\sigma_y - 0.26\sigma_{Tastm} - 0.109\sigma_{Lastm}. \quad [4]$$

2. Temperature distribution

The temperature profile obtained from the numerical analysis is shown in Figure 7. It shows the temperature profile for the root pass, 1st pass, 11th pass, 12th pass, and final pass (14th). The temperature profile is represented by the weld fusion zone of conventional V-groove design, as shown in Figure 7. The temperature profile for the root pass is predicted at the point of interest in the middle of the root weld, as shown in Figure 7(a). The temperature profile is shown for a time of 214 seconds. For the root pass, at the center of the weld zone, the peak temperature reaches about 2080 °C, which is higher than the P91 steel melting temperature. The peak temperature then decreases below 100 °C within 100 seconds. The root pass is further affected by the subsequent passes' heat input, and the temperature reaches 1354 °C for the 1st pass in the analysis period of 214 seconds. Figure 7(b) shows the temperature profile for the point of interest in the 1st pass. The 1st pass is affected by the root pass where the preheating effect occurs. The preheating temperature for the 1st pass was calculated to be 360 °C. The peak temperature for the 1st pass exceeds 2000 °C, as shown in Figure 7(b). The temperature profiles for the 11th, 12th, and final pass are shown in Figures 7(c) through (e), respectively. The peak temperatures during the 11th, 12th, and final pass were 2440 °C, 2485 °C, and 2075 °C, respectively.

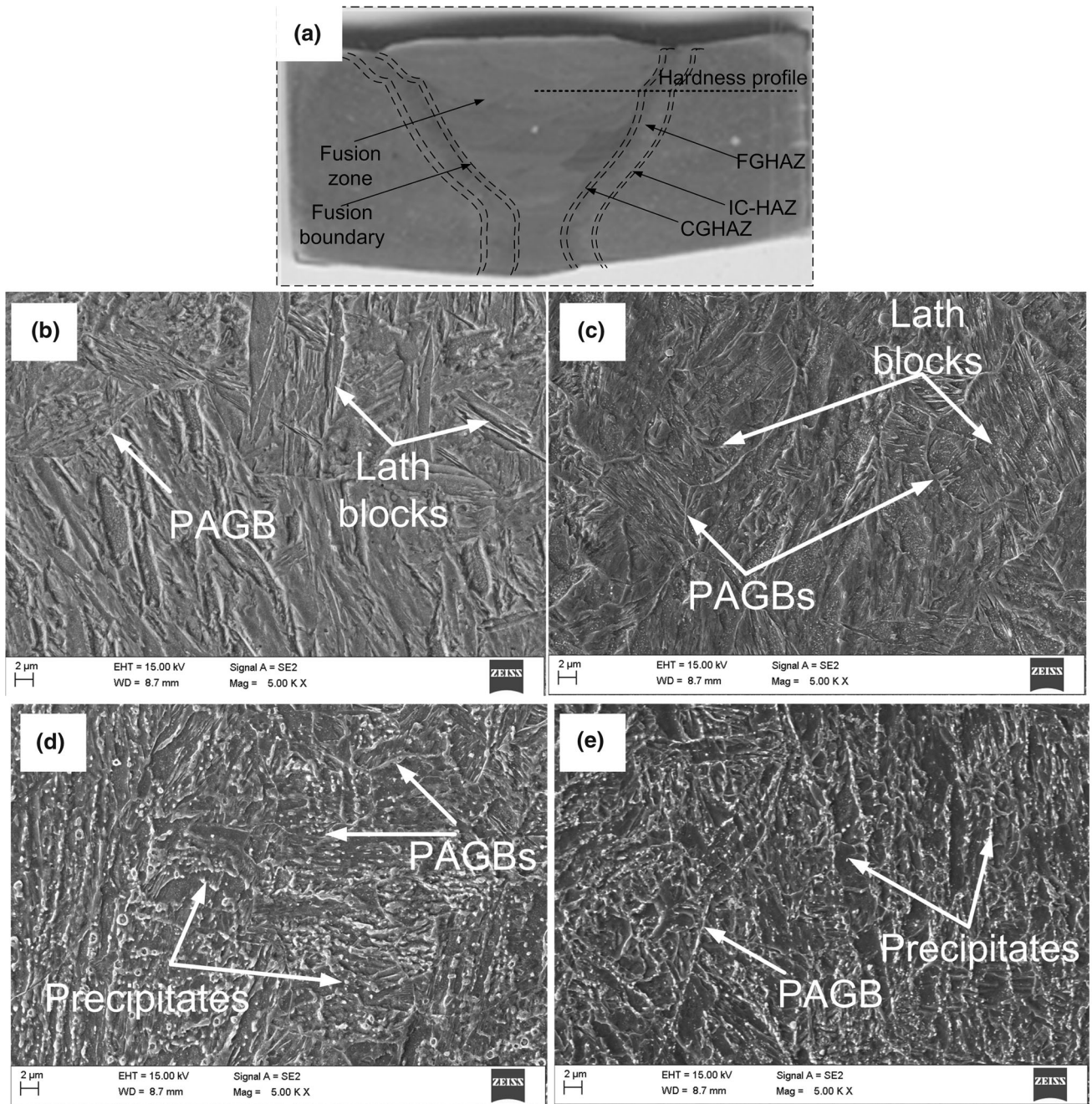


Fig. 5—(a) Cross section of multipass welded butt joint (case I); secondary electron micrograph of subzones of P91 weldments: (b) weld fusion zone, (c) CGHAZ, (d) FGHAZ, and (e) IC-HAZ.

Figure 7 shows that the peak temperature during each welding pass exceeds the melting temperature of the material. However, all the points in the weld fusion zone do not reach the same peak temperature.

3. Results of structural analysis of conventional V groove

The results obtained from the thermal analysis were used to perform the nonlinear elasto-plastic structural analysis, using the following stress-strain Eqs. [5] through [7].^[43]

$$\{\sigma\} = [D]\{\varepsilon^e\}, \quad [5]$$

where

$$\{\varepsilon^e\} = \{\varepsilon\} - \{\varepsilon^f\}, \quad [6]$$

$$\{\varepsilon^f\} = \Delta T[\alpha_x, \alpha_y, \alpha_z, 0, 0, 0]^T, \quad [7]$$

where $\Delta T = T_n - T_\infty$ and T_n is the temperature at the point of interest. In the case of nonlinear materials, total strain can be written as

$$\{\varepsilon\} = \{\varepsilon^e\} + \{\varepsilon^t\} + \{\varepsilon^p\}. \quad [8]$$

In Eq. [8], the right-side components are elastic strain, thermal strain, and plastic strain, respectively.

The numerical simulation was performed for case I. After the structure analysis, the simulated axial and transverse residual stresses were predicted. The distributions of axial and transverse residual stresses are shown in Figures 8(a) and (b), respectively. In the weld fusion zone, unsymmetrical distribution of axial and transverse residual stresses is clearly observed. The predicted axial and transverse stresses show tensile behavior at the outer surfaces of the welded plate, while the compressive nature of stresses was observed at the inner surfaces. The range of stress is observed to be lower in the circumferential direction than in the axial one. The outer surface of the welded plate shows the maximum axial stress at the weld center. At the inner surfaces (near the weld centerline), the magnitude of residual stresses was observed to be much lower.

Experimentally measured residual stresses at the outer surface of P91 welded plate compared fairly well with the numerically obtained residual stress value. Figure 9 shows the peak axial and transverse residual stresses near the weld center. The experimentally measured peak axial and transverse residual stresses were 102 and 196 MPa, as shown in Table VI. A lower value of

residual stresses was measured in the HAZ, as shown in Table VI. The compressive nature of residual stresses was measured in the root section. In Figure 9, the tensile nature of residual stresses in the weld zone and HAZ are confirmed, while the compressive nature in the root is measured. The predicted residual stress value matched the numerically obtained residual stresses at the outer surfaces and at the root section. However, some discrepancy was observed between simulated and experimental results at the weld center for both axial and transverse stresses.

C. Flexural Stress

1. Top side

Three-point bending tests were performed at room temperature for both the face and root sides. The fractured three-point bend test specimens for the face side are shown in Figure 10(a). The results of the flexural tests are depicted in Table VII. In the as-welded condition, the weld fusion zone consists of the brittle martensitic structure. In case I, the fracture occurs from the weld fusion zone, as shown in Figure 10(a). In case II, the bending angle reaches 180 deg with a crack along the weld fusion boundary or CGHAZ. In cases III and IV, porosity is clearly seen in the weld fusion zone. Porosity present in the fusion zone acted as the stress concentrator during the flexural test, and failure mainly occurred due to the crack initiated from the porosity. In cases III and IV, the fracture was noticed in the fusion zone. The complete brittle fracture was noticed in cases III and IV. In cases I, III, and IV, the fracture was noticed in the weld fusion zone, while in case II, the fracture was noticed in the fusion line. Guo *et al.*^[44] also reported the fracture of the welded joint in the fusion zone during the three-point bending test on the face side. Li *et al.*^[45] also reported the failure of the welded joint from the fusion zone during the three-point bending test of the face side. The microcracks would be subjected to compressive stress during the face bending test and would not propagate easily.

Flexural strengths measured for cases I, II, III, and IV were 1621, 1616, 1524, and 1424 MPa, respectively. Flexural strength was found to decrease with a change in electrode condition from case I to case IV. The main reason for the decrement was the presence of diffusible

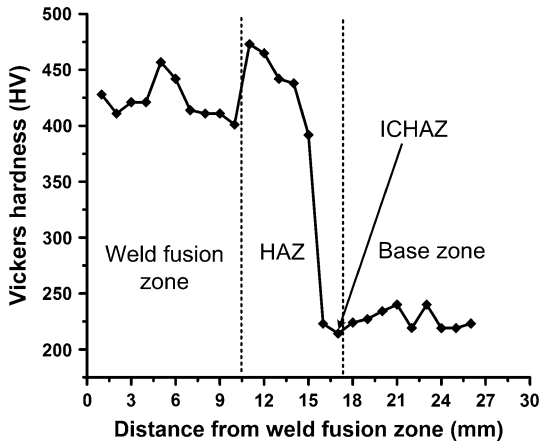


Fig. 6—Hardness distribution in transverse direction from weld fusion zone to overtempered base metal.

Table VI. Residual Stress Results in P91 Welded Plate

Specimen	Residual Stress at Weld Center (MPa)		Residual Stress at 4 mm away from Center (MPa)		Residual Stress in HAZ (MPa)		Residual Stress in Root (MPa)	
	Axial Stress ASTM/Corrected Value	Transverse Stress ASTM/Corrected Value	Axial Stress ASTM/Corrected Value	Transverse Stress ASTM/Corrected Value	Axial Stress ASTM/Corrected Value	Transverse Stress ASTM/Corrected Value	Axial Stress ASTM/Corrected Value	Transverse Stress ASTM/Corrected Value
Case I	205/102	295/196	189/92	170/82	196/97	151/69	- 69/- 78	- 100/- 62
Case II	145/61	355/205	164/75	143/67	183/88	145/66	- 88/- 90	- 123/- 76
Case III	192/93	305/168	173/81	143/66	154/68	231/124	- 137/- 123	- 116/- 65
Case IV	218/110	271/143	196/97	171/82	163/75	149/71	- 157/- 137	- 105/- 56

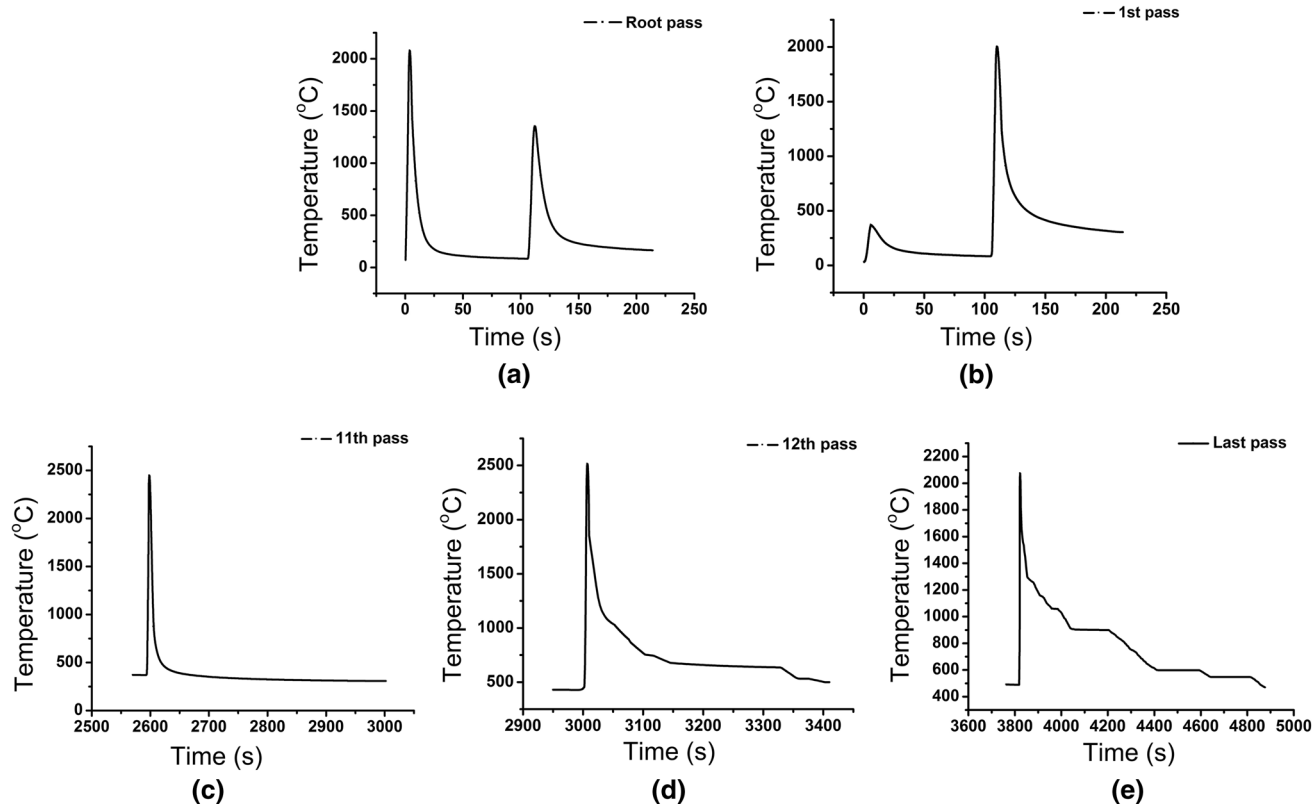


Fig. 7—Predicted temperature distributions of (a) root pass weld, (b) 1st pass weld, (c) 11th weld pass, (d) 12th pass, and (e) 14th weld pass (last pass).

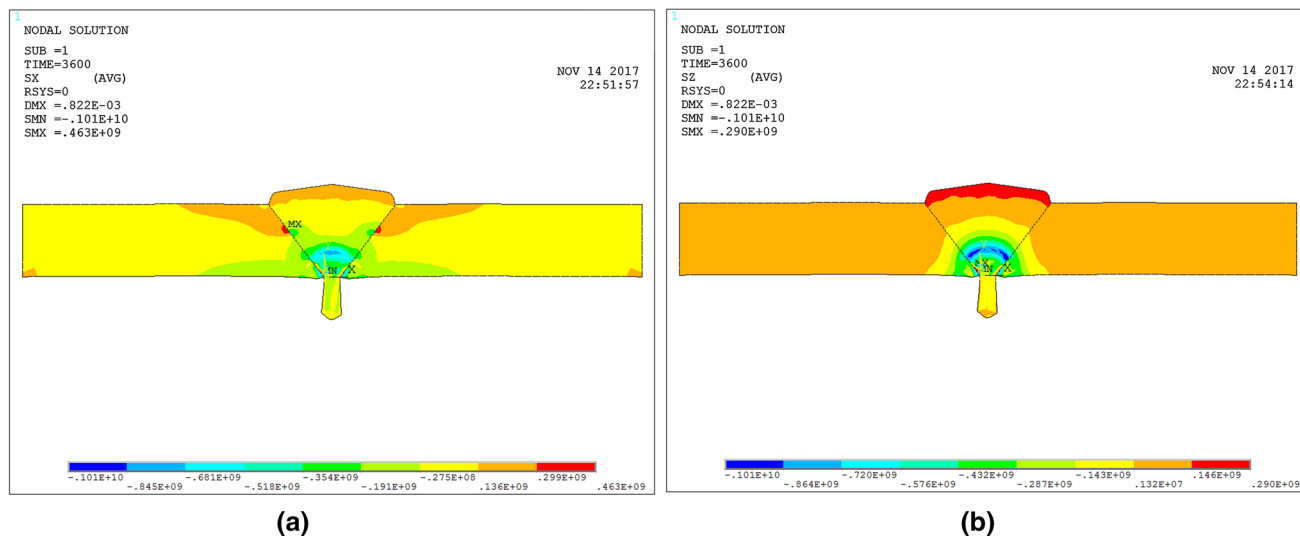


Fig. 8—(a) Simulated axial residual stress distribution for conventional groove and (b) simulated transverse residual stress distribution for conventional groove.

hydrogen in the weld fusion zone for cases III and IV. The electrodes used in the backed condition and the as-supplied condition produced similar results. The weld fusion zone has a martensitic structure for each case, but a change in electrode condition introduced porosity and some other type of defects in the weld

fusion zone. The engineering stress-strain curve for the three-point face bending of the multipass butt-welded joint is shown in Figure 11(a). As shown in Figure 11(a), the fracture noticed in cases III and IV was brittle mode, while for cases I and II, yielding was noticed. In cases II and III, a sudden dip in the curve

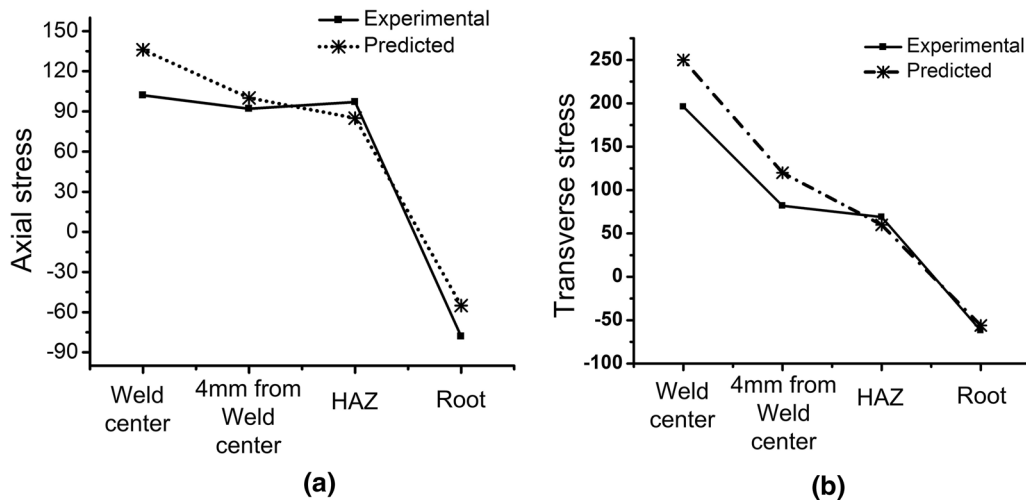


Fig. 9—Numerical and experimental value of residual stresses in P91 welded plate: (a) axial stress and (b) transverse stress.

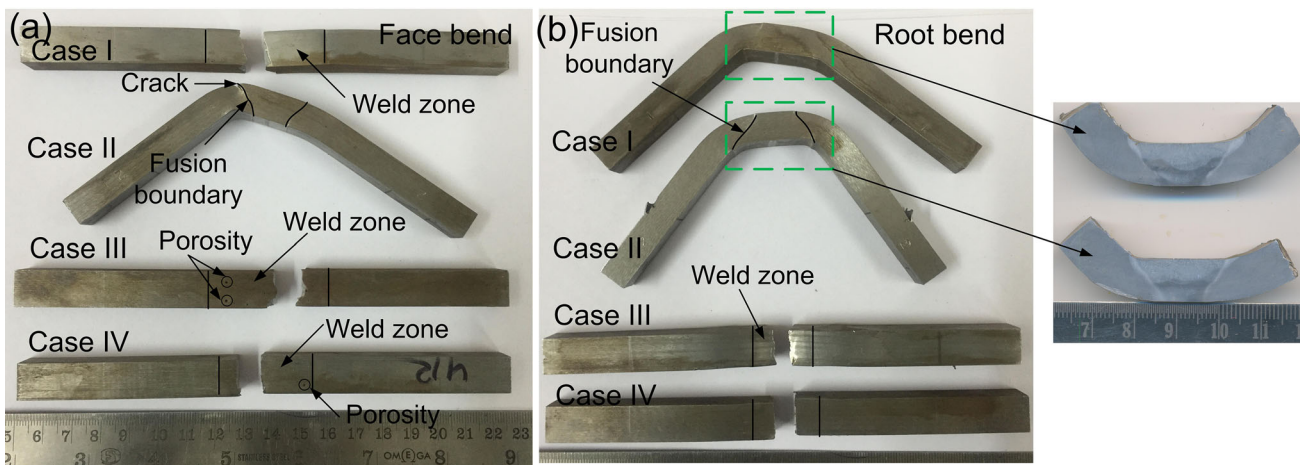


Fig. 10—Three-point bending test specimens (a) for face side and (b) for root side.

Table VII. Result of Flexural Tests

Specimen	Face Side			Root Side		
	Flexural Strength (MPa)	Percent Elongation	Load (kN)	Flexural Strength (MPa)	Percent Elongation	Load (kN)
Case I	1621	25.62	13.78	1702	22.53	14.47
Case II	1616	23.38	13.6	1642	27.52	13.97
Case III	1524	13.45	13.06	1393	4.55	12.09
Case IV	1445	5.1	12.85	1234	2.9	10.49

(highlighted with a green circle) was noticed. The sudden dip in the flexural curve shows the presence of porosity of smaller size from which cracks were initiated but not converted into the final fracture. In case I, no sudden dip was noticed, indicating the porosity of the free weld fusion zone for this case. The

percent elongations measured for cases I and IV were 25.62 and 5.1 pct, respectively. Hence, the presence of porosity in the weld fusion zone affects the ductility of material to a great extent. As the level of hydrogen increased in the electrode, the percent elongation was found to decrease for face bending tests.

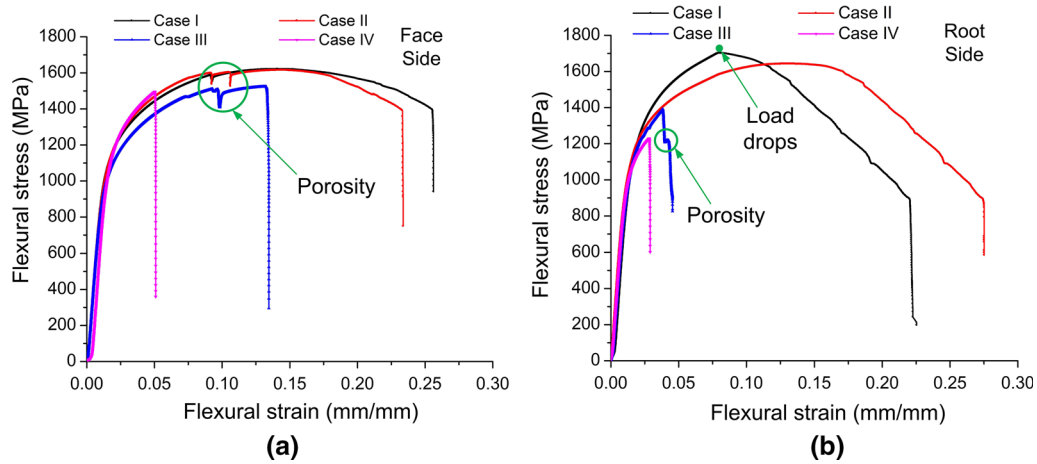


Fig. 11—Three-point bending test results performed at room temperature for multipass welded joint of P91 steel: (a) face side and (b) root side.

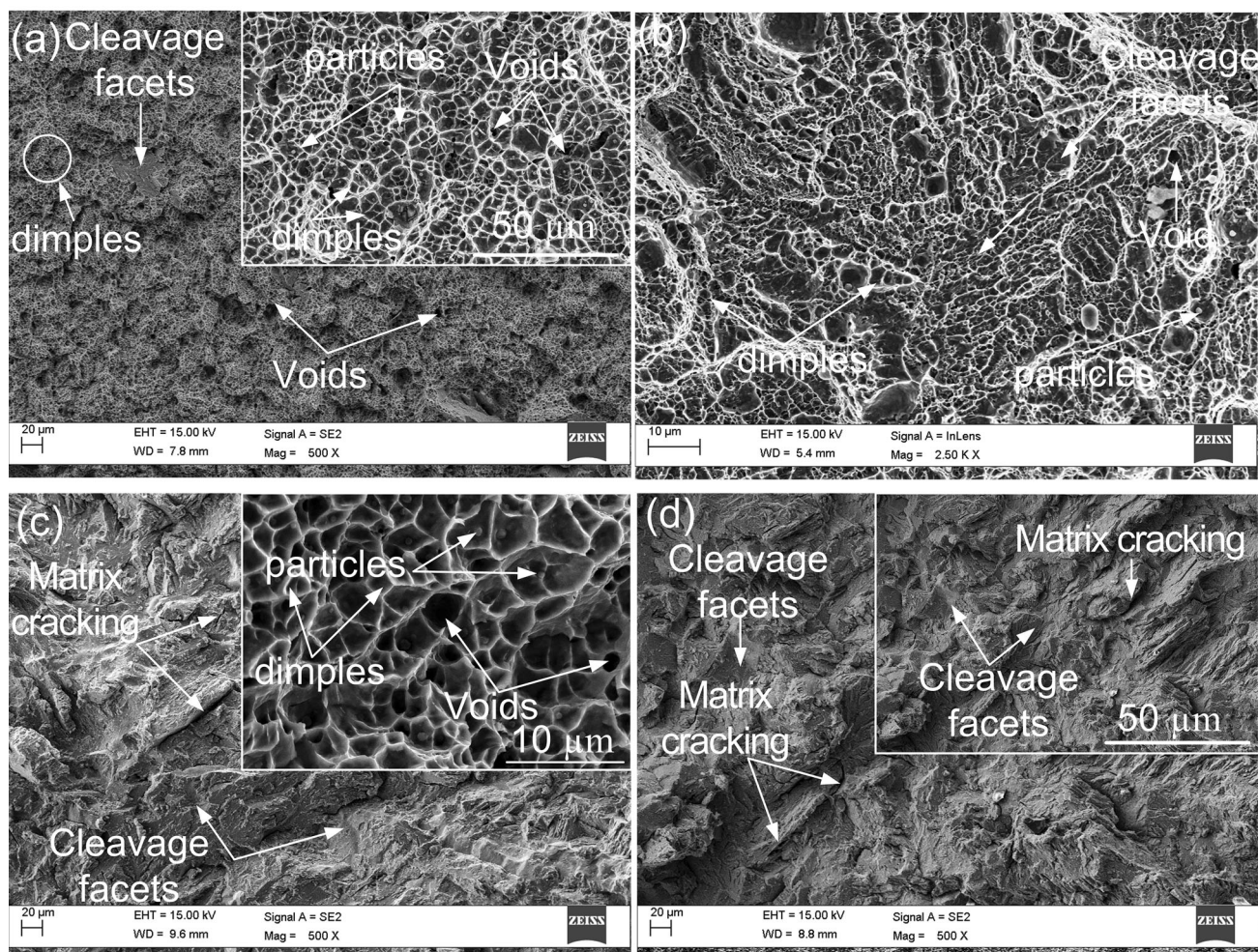


Fig. 12—Secondary electron micrograph of fractured three-point bend test specimens for face side: (a) case I, (b) case II, (c) case III, and (d) case IV.

2. Root side

The fractured three-point bend test specimens for the face side are shown in Figure 10(b). The three-point root bending test plot for the different conditions of the electrode is shown in Figure 11(b). Maximum flexural strength was noticed at about 1702 MPa for case I. For cases I and II, the fracture occurred with yielding, but in cases III and IV, no yielding was noticed. The sudden fracture for cases III and IV looks similar to the face bend test and provides the brittle mode of fracture. In cases I and II, the complete yielding occurred without any crack. The flexural strength measured for case IV was 1234 MPa, which was much less than that in case I. The ductilities measured for cases III and IV were 4.55 and 2.9 pct, respectively, which were also much less than those in cases I and II. The fluctuation in curve was noticed due to the presence of minute porosity in the weld fusion zone. Guo *et al.*^[44] reported the fracture in the fusion line for root bend tests.

D. Fractographs After the Flexural Test

The fractographs of the flexural test specimen are shown in Figures 12(a) through (d). In case I, the crack initiation zone revealed the ductile dimples, the fewer amount of cleavage facets, and some small size voids, as shown in Figure 12(a). The final fracture zone is shown in the top right of Figure 12(a). The final fracture surface revealed the ductile mode of fracture, and both voids and dimples were seen on the fractographs. In the final fracture zone, small size particles were distributed uniformly inside the ductile dimples. In case II, the final fracture zone showed a mixed mode of fracture. Cleavage facets and ductile dimples were both noticed on the fracture surface. In case II, the number of voids was found to increase as compared to that in case I. In case III, the crack initiation zone was characterized by cleavage facets with matrix cracking, as shown in Figure 12(c). The final fracture zone still shows the ductile fracture mode and is characterized by ductile dimples and microvoids as compared to cases I and II. In case IV, an interesting pattern of fracture was observed. The crack initiation and final fracture zones were characterized by cleavage facets and matrix cracking.

The MnS particles may act as crack nucleation sites because of brittleness. The Cr-rich $M_{23}C_6$ and V- and Nb-rich MX particles may also act as stress concentrators. The segregation of S along the crack tip was reported by Hipsley.^[46] Wedge crack formation in plain 9Cr-1Mo steel, due to the splitting of lath boundaries, was reported by Choudhary and Samuel.^[47] The presence of silicon and phosphorous in P91 steel promoted the splitting of lath boundaries. A higher percentage of phosphorous in P91 steel makes it susceptible to phosphorous embrittlement.^[48]

IV. CONCLUSIONS

In the present research, the P91 steel weld joint was prepared for four different conditions of weld consumables that provided a different level of diffusible hydrogen. The P91 steel weld joints were subjected to top and root flexural bend tests. The axial and transverse residual stresses were also measured experimentally in different welded plates using the blind hole drilling method. The experimentally obtained residual stresses were matched fairly well with numerically obtained results for case I (low level of diffusible hydrogen). The different conditions of weld consumables or diffusible hydrogen contents did not have any significant effect on axial and transverse residual stresses. The axial and transverse shrinkage stresses were measured at different locations, *i.e.*, the center of the weld fusion zone, 4 mm away from the weld fusion zone, and HAZ. In each location, the residual stresses were observed to be tensile in nature. However, the maximum magnitude of residual stresses was measured at the center of the weld fusion zone. The maximum value of transverse stress was measured to be 355 MPa for case II, while the maximum axial stress was about 218 MPa for case IV. The transverse and axial stresses measured in the root of the welded plate were observed to be compressive in nature. In numerical analysis, residual stresses showed unsymmetrical distributions in the weld fusion zone. The predicted residual stress value matched fairly well with the numerically obtained residual stresses at the outer surfaces and at the root section. However, some discrepancy was observed between simulated and experimental results at the weld center for both axial and transverse stresses.

REFERENCES

1. A. Aghajani, C. Somsen, and G. Eggeler: *Acta Mater.*, 2009, vol. 57, pp. 5093–5106.
2. C. Pandey and M.M. Mahapatra: *J. Mater. Eng. Performance*, 2016, vol. 25, pp. 2195–2210.
3. C. Pandey, M.M. Mahapatra, P. Kumar, R.S. Vidyrathy, and A. Srivastava: *Mater. Sci. Eng. A*, 2017, vol. 695, pp. 291–301.
4. M. Dewitte and C. Coussement: *Mater. High Temp.*, 1991, vol. 9, pp. 178–84.
5. I. Fedorova, A. Kipelova, A. Belyakov, and R. Kaibyshev: *Metall. Mater. Trans. A*, 2018, vol. 49A.
6. B. Silwal, L. Li, A. Deceuster, and B. Griffiths: *Weld. Res.*, 2013, vol. 92, pp. 80s–87s.
7. X. Li, M.T. Cabrilhat, and Y. Lejeail: *Study Modif. 9Cr-1Mo Welds*, 2006, vol. 43.
8. G.A. Webster and A.N. Ezeilo: *Int. J. Fatigue*, 2001, vol. 23, pp. 375–83.
9. P. Dong and P. Dong: *Sci. Technol. Weld. Join.*, 2004, vol. 10, pp. 389–98.
10. P.G. Kumar and K. Yu-ichi: *Trans. JWRI*, 2013, vol. 42, pp. 39–62.
11. C. Pandey, M.M. Mahapatra, and P. Kumar: *Arch. Civil Mech. Eng.*, 2018, vol. 18, pp. 1000–11.
12. A.H. Yaghi, T.H. Hyde, A.A. Becker, and W. Sun: *IMechE*, 2008, vol. 43, pp. 275–93.

13. M. Zubairuddin, S.K. Albert, M. Vasudevan, S. Mahadevan, V. Chaudhri, and V.K. Suri: *Mater. Manuf. Process.*, 2016, vol. 31, pp. 366–71.
14. D. Dean and M. Hidekazu: *Comput. Mater. Sci.*, 2006, vol. 37, pp. 209–19.
15. H. Murakawa, B. Miloslav, V. Adan, R. Sherif, and D. Cartin: *Trans. JWRI*, 2008, vol. 37, pp. 75–80.
16. S. Paddea, J.A. Francis, A.M. Paradowska, P.J. Bouchard, and I.A. Shibli: *Mater. Sci. Eng. A*, 2012, vol. 534, pp. 663–72.
17. J.A. Francis, W. Mazur, and H.K.D.H. Bhadeshia: *Mater. Sci. Technol.*, 2006, vol. 22, pp. 1387–95.
18. K.A. Venkata, S. Kumar, H.C. Dey, D.J. Smith, and P.J. Bouchard: *Proc. Eng.*, 2014, vol. 86, pp. 223–33.
19. T.C. Chuvas, P.S.P. Garcia, J.M. Pardal, and P.C. da Fonseca: *Mater. Res.*, 2015, vol. 18, pp. 614–21.
20. S. Kulkarni, P.K. Ghosh, and S. Ray: *ISIJ Int.*, 2008, vol. 48, pp. 1560–69.
21. S. Kim, J. Kim, and W. Lee: *J. Mater. Process. Technol.*, 2009, vol. 209, pp. 3905–13.
22. Y. Sattari-Far and I. Javadi: *Int. J. Press. Vess. Pip.*, 2008, vol. 85, pp. 265–74.
23. P. Dong: *J. Press. Vess. Technol.*, 2001, vol. 123, pp. 207–13.
24. N. Saini, C. Pandey, and M.M. Mahapatra: *Int. J. Hydrog. Energy*, 2017, vol. 42, pp. 17328–38.
25. C. Pandey, M.M. Mahapatra, P. Kumar, and N. Saini: *J. Eng. Mater. Technol.*, 2017, vol. 139, pp. 1–11.
26. S.K. Albert, V. Ramasubbu, S.I.S. Raj, and A.K. Bhaduri: *Weld. World*, 2011, vol. 55, pp. 66–74.
27. X. Yue: *Weld. World*, 2014, vol. 59, pp. 77–89.
28. C. Pandey, M.M. Mahapatra, P. Kumar, N. Saini, A. Srivastava: *J. Manuf. Process.*, 2017, vol. 28, pp. 220–34.
29. C. Pandey, M.M. Mahapatra, P. Kumar, and N. Saini: *Trans. Ind. Inst. Met.*, 2017, <https://doi.org/10.1007/s12666-017-1144-4>.
30. J.N. Dupont and A.R. Marder: *Weld. Res. Suppl.*, 1995, vol. 74, pp. 406–16.
31. C. Pandey, A. Giri, and M.M. Mahapatra: *Int. J. Steel Struct.*, 2016, vol. 16, pp. 333–45.
32. C. Pandey, N. Saini, M.M. Mahapatra, and P. Kumar: *Int. J. Hydrogen Energy*, 2016, vol. 41, pp. 17695–71712.
33. A. Giri, C. Pandey, M.M. Mahapatra, K. Sharma, and P.K. Singh: *Meas.: J. Int. Meas. Confed.*, 2015, vol. 65, pp. 41–49.
34. A.H. Yaghi, T.H. Hyde, A.A. Becker, W. Sun, G. Hilsen, S. Simandjuntak, P.E.J. Flewitt, and D.J. Smith: *J. Press. Vess. Technol.*, 2010, vol. 132, pp. 1–10.
35. L.X. Jang, X.F. Peng, and B.X. Wang: *Int. J. Heat Mass Transf.*, 2001, vol. 44, pp. 4465–73.
36. J. Goldak: *Metall. Trans. A*, 1986, vol. 17A, pp. 17–26.
37. B. Brickstad and B.L. Josefson: *Int. J. Press. Vess. Pip.*, 1998, vol. 75, pp. 11–25.
38. C. Liu, J.X. Zhang, and C.B. Xue: *Fus. Eng. Design*, 2011, vol. 86, pp. 288–95.
39. C. Pandey, N. Saini, M.M. Mahapatra, and P. Kumar: *Eng. Fail. Anal.*, 2016, vol. 71, pp. 131–47.
40. C. Pandey, A. Giri, M.M. Mahapatra, and P. Kumar: *Met. Mater. Int.*, 2017, vol. 23, pp. 148–62.
41. Y. Wang, R. Kannan, and L. Li: *Metall. Mater. Trans. A*, 2016, vol. 47A, pp. 5680–84.
42. C. Pandey and M.M. Mahapatra: *J. Mater. Eng. Perform.*, 2016, vol. 25, pp. 2761–75.
43. M.M. Mahapatra, G.L. Datta, B. Pradhan, and N.R. Mandal: *Int. J. Press. Vess. Pip.*, 2006, vol. 83, pp. 721–29.
44. N. Guo, Z. Yang, M. Wang, X. Yuan, and J. Feng: *Strength Mater.*, 2015, vol. 47, pp. 12–18.
45. H.L. Li, D. Liu, Y.T. Yan, N. Guo, and J.C. Feng: *J. Mater. Process. Technol.*, 2016, vol. 238, pp. 423–30.
46. C.A. Hippsley: *Acta Metall.*, 1987, vol. 35, pp. 2399–2416.
47. B.K. Choudhary and E. Isaac: *Samuel J. Nucl. Mater.*, 2011, vol. 412, pp. 82–89.
48. S. Sathyanarayanan, A. Moitra, K.G. Samuel, G. Sasikala, S.K. Ray, and V. Singh: *Mater. Sci. Eng. A*, 2008, vol. 488, pp. 519–28.